



# Observation and confirmation of nine strong-lensing systems in Dark Energy Survey Year 1 data

B. Nord<sup>1,2,3\*</sup>, E. Buckley-Geer,<sup>1</sup> H. Lin,<sup>1</sup> N. Kuropatkin,<sup>1</sup> T. Collett<sup>1,4</sup>, D. L. Tucker,<sup>1</sup> H. T. Diehl,<sup>1</sup> A. Agnello,<sup>5</sup> A. Amara,<sup>6</sup> T. M. C. Abbott,<sup>7</sup> S. Allam,<sup>1</sup> J. Annis,<sup>1</sup> S. Avila<sup>1,4</sup>, K. Bechtol,<sup>8,9</sup> D. Brooks,<sup>10</sup> D. L. Burke,<sup>11,12</sup> A. Carnero Rosell,<sup>13,14</sup> M. Carrasco Kind<sup>1,15,16</sup>, J. Carretero,<sup>17</sup> C. E. Cunha,<sup>11</sup> L. N. da Costa,<sup>14,18</sup> C. Davis<sup>1,11</sup>, J. De Vicente,<sup>13</sup> P. Doel,<sup>10</sup> T. F. Eifler,<sup>19,20</sup> A. E. Evrard<sup>1,21,22</sup>, E. Fernandez,<sup>17</sup> B. Flaugher,<sup>1</sup> P. Fosalba,<sup>23,24</sup> J. Frieman,<sup>1,2</sup> J. García-Bellido,<sup>25</sup> E. Gaztanaga<sup>1,23,24</sup>, D. Gruen<sup>1,11,12,26</sup>, R. A. Gruendl,<sup>15,16</sup>, G. Gutierrez,<sup>1</sup> W. G. Hartley,<sup>6,10</sup>, D. L. Hollowood,<sup>27</sup> K. Honscheid,<sup>28,29</sup>, B. Hoyle<sup>1,30,31</sup>, D. J. James,<sup>32</sup> K. Kuehn,<sup>33</sup> O. Lahav,<sup>10</sup> M. Lima,<sup>14,34</sup>, M. A. G. Maia,<sup>14,18</sup> M. March<sup>1,35</sup>, J. L. Marshall,<sup>36</sup> P. Melchior,<sup>37</sup> F. Menanteau,<sup>15,16</sup>, R. Miquel,<sup>17,38</sup> A. A. Plazas<sup>1,20</sup>, A. K. Romer,<sup>39</sup> A. Roodman,<sup>11,12</sup> E. S. Rykoff,<sup>11,12</sup>, E. Sanchez,<sup>13</sup> V. Scarpine,<sup>1</sup> R. Schindler,<sup>12</sup> M. Schubnell,<sup>22</sup> I. Sevilla-Noarbe,<sup>13</sup>, M. Smith<sup>1,40</sup>, M. Soares-Santos,<sup>41</sup> F. Sobreira,<sup>14,42</sup> E. Suchyta<sup>1,43</sup>, M. E. C. Swanson,<sup>16</sup>, G. Tarle,<sup>22</sup> D. Thomas<sup>1,4</sup>, Y. Zhang<sup>1</sup> and (DES Collaboration)

*Affiliations are listed at the end of the paper*

Accepted 2019 October 30. Received 2019 October 30; in original form 2019 February 8

## ABSTRACT

We describe the observation and confirmation of nine new strong gravitational lenses discovered in Year 1 data from the Dark Energy Survey (DES). We created candidate lists based on (i) galaxy group and cluster samples, and (ii) photometrically selected galaxy samples. We selected 46 candidates through visual inspection and then used the Gemini Multi-Object Spectrograph (GMOS) at the Gemini South telescope to acquire a spectroscopic follow-up of 21 of these candidates. Through an analysis of these spectroscopic follow-up data, we confirmed nine new lensing systems and rejected two candidates, and the analysis was inconclusive on 10 candidates. For each of the confirmed systems, our report measured spectroscopic properties, estimated source image–lens separations, and estimated enclosed masses as well. The sources that we targeted have an *i*-band surface brightness range of  $i_{\text{SB}} \sim 22\text{--}24 \text{ mag arcsec}^{-2}$  and a spectroscopic redshift range of  $z_{\text{spec}} \sim 0.8\text{--}2.6$ . The lens galaxies have a photometric redshift range of  $z_{\text{lens}} \sim 0.3\text{--}0.7$ . The lensing systems range in source image–lens separation from 2 to 9 arcsec and in enclosed mass from  $10^{12}$  to  $10^{13} \text{ M}_{\odot}$ .

**Key words:** gravitational lensing: strong – techniques: spectroscopic – galaxies: individual.

## 1 INTRODUCTION

Strong gravitational lensing uniquely demonstrates the interplay between energy and space–time. The light rays from background sources, like galaxies and quasars, are deflected by massive dark

matter haloes that are in alignment along an observer’s line of sight, producing highly distorted images of these sources. In this role, strong lensing provides opportunities to study multiple astrophysical and cosmological phenomena – from the evolution of highly magnified distant galaxies in the early Universe to the matter distribution on the scales of galaxies, as well as cosmic acceleration (see Treu 2010).

\* E-mail: [nord@fnal.gov](mailto:nord@fnal.gov)

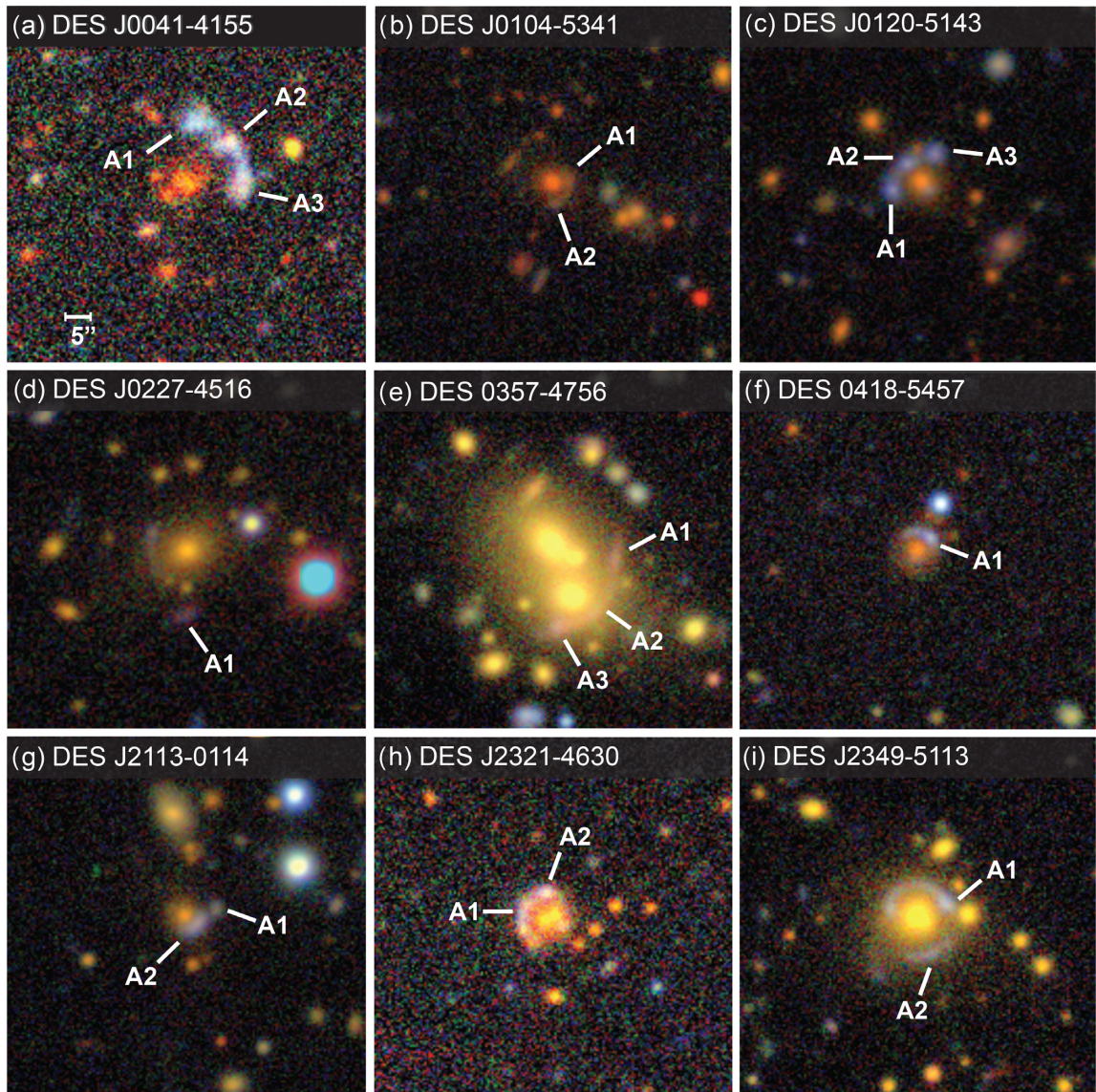


**Figure 1.** Colour co-add DES images of the nine confirmed lensing systems described in this work: (a) DES J0041–4155, (b) DES J0104–5341, (c) DES J0120–5143, (d) DES J0227–4516, (e) DES J0357–4756, (f) DES J0418–5457, (g) DES J2113–0114, (h) DES J2321–4630, and (i) DES J2349–5113. Images are oriented north up, east left, and are  $1 \times 1$  arcmin $^2$  in area. The colour images are composites of the  $g$ ,  $r$ , and  $i$  bands. The lensing features targeted for spectroscopy are indicated by the letters. Refer to Figs 2–10 for additional images of the candidates and their spectroscopic information.

About a thousand lensing systems have been discovered over the last few decades, which we detailed in Nord et al. (2016). Modern large-scale surveys have the potential to increase the sample by orders of magnitude by virtue of their relatively large depth and sky area. For example, based on selection-function estimates of spectroscopic confirmations (see Nord et al. 2016) and simulation-based forecasts of future surveys (see Collett et al. 2012), the Dark Energy Survey (DES<sup>1</sup>; Diehl et al. 2014; Flaugher et al. 2015; Dark Energy Survey Collaboration et al. 2016) is likely to observe more than 2000 galaxy- and cluster-scale lensing systems with arcs, and over a hundred lensed quasars (see Oguri & Marshall 2010). The Large Synoptic Survey Telescope (LSST<sup>2</sup>; Ivezić et al. 2008) data

will contain an order of magnitude more (Oguri & Marshall 2010; Collett 2015)

Each species of strong lens – characterized by the scale of the lens, the objects being lensed, and image morphology – has particular strengths for studying the dark matter, dark energy, cosmic expansion rate, galaxy evolution, and other phenomena. For example, modelling individual lens systems can constrain mass profiles and mass-to-light ratios of early-type galaxies (see Sonnenfeld et al. 2013). Modelling the population of galaxy- and group-scale lenses can become constraints on profiles of dark matter haloes in lenses (see More et al. 2012, 2016). Double-source-plane lenses – when there are two sources along the line of sight behind a lens – can constrain cosmic dark matter and dark energy densities, largely independent of the Hubble constant (Collett 2015; Linder 2016). To this date, only a few have been discovered (e.g. Gavazzi et al. 2008; Tanaka et al. 2016). Time-delay cosmology uses variable

<sup>1</sup>[darkenergysurvey.org](https://darkenergysurvey.org)

<sup>2</sup>[lsst.org](https://lsst.org)

**Table 1.** Properties of lensing systems: positions and photometry of lenses and source images.

Object name	RA (J2000) ( $^{\circ}$ )	Dec. (J2000) ( $^{\circ}$ )	$(g, r, i, z, Y)$
DES J0041–4155	10.276756	–41.926677	(24.55 $\pm$ 00.28, 22.39 $\pm$ 00.04, 21.12 $\pm$ 00.02, 20.62 $\pm$ 00.02, 20.22 $\pm$ 00.10)
A1	10.276189	–41.924554	(22.65 $\pm$ 00.05, 22.16 $\pm$ 00.03, 22.15 $\pm$ 00.05, 21.98 $\pm$ 00.07, 21.82 $\pm$ 00.42)
A2	10.274828	–41.925309	(22.73 $\pm$ 00.05, 22.12 $\pm$ 00.03, 21.72 $\pm$ 00.03, 21.43 $\pm$ 00.04, 20.99 $\pm$ 00.19)
A3	10.274230	–41.926661	(22.77 $\pm$ 00.06, 22.30 $\pm$ 00.03, 21.85 $\pm$ 00.04, 21.73 $\pm$ 00.06, 21.92 $\pm$ 00.45)
DES J0104–5341	16.098363	–53.699436	(23.42 $\pm$ 00.05, 21.45 $\pm$ 00.01, 20.31 $\pm$ 00.01, 19.85 $\pm$ 00.01, 19.93 $\pm$ 00.04)
A1*	16.097533	–53.699283	(24.22 $\pm$ 00.08, 22.85 $\pm$ 00.04, 21.95 $\pm$ 00.03, 21.36 $\pm$ 00.02, 21.42 $\pm$ 00.02)
A2	16.098237	–53.700129	(24.14 $\pm$ 00.10, 23.08 $\pm$ 00.05, 22.46 $\pm$ 00.05, 21.86 $\pm$ 00.06, 22.22 $\pm$ 00.28)
DES J0120–5143	20.175979	–51.731407	(22.52 $\pm$ 00.02, 20.82 $\pm$ 00.01, 19.97 $\pm$ 00.01, 19.54 $\pm$ 00.01, 19.50 $\pm$ 00.02)
A1	20.177571	–51.731638	(21.91 $\pm$ 00.01, 21.65 $\pm$ 00.01, 21.44 $\pm$ 00.02, 21.00 $\pm$ 00.02, 21.03 $\pm$ 00.08)
A2	20.176720	–51.730802	(21.83 $\pm$ 00.01, 21.43 $\pm$ 00.01, 21.16 $\pm$ 00.01, 20.69 $\pm$ 00.02, 20.73 $\pm$ 00.06)
A3	20.175358	–51.730461	(22.03 $\pm$ 00.01, 21.71 $\pm$ 00.02, 21.46 $\pm$ 00.02, 21.03 $\pm$ 00.03, 21.11 $\pm$ 00.08)
DES J0227–4516	36.790976	–45.275305	(20.45 $\pm$ 00.02, 18.75 $\pm$ 00.01, 18.10 $\pm$ 00.01, 17.75 $\pm$ 00.01, 17.54 $\pm$ 00.02)
A1	36.792491	–45.274846	(22.58 $\pm$ 00.05, 21.79 $\pm$ 00.04, 21.22 $\pm$ 00.04, 20.93 $\pm$ 00.06, 20.65 $\pm$ 00.13)
DES J0357–4756	59.307522	–47.946327	(20.66 $\pm$ 00.00, 19.07 $\pm$ 00.00, 18.58 $\pm$ 00.00, 18.14 $\pm$ 00.00, 18.03 $\pm$ 00.01)
A1*	59.304217	–47.946867	(23.14 $\pm$ 00.05, 22.24 $\pm$ 00.03, 21.69 $\pm$ 00.02, 21.35 $\pm$ 00.02, 21.27 $\pm$ 00.02)
A2*	59.305462	–47.948650	(22.57 $\pm$ 00.04, 21.32 $\pm$ 00.02, 20.80 $\pm$ 00.02, 20.49 $\pm$ 00.01, 20.31 $\pm$ 00.01)
A3*	59.307237	–47.949167	(22.48 $\pm$ 00.03, 21.60 $\pm$ 00.02, 21.06 $\pm$ 00.02, 20.72 $\pm$ 00.02, 20.60 $\pm$ 00.01)
DES J0418–5457	64.541167	–54.959729	(23.51 $\pm$ 00.06, 21.84 $\pm$ 00.02, 20.95 $\pm$ 00.01, 20.50 $\pm$ 00.02, 20.40 $\pm$ 00.05)
A1	64.540461	–54.959360	(22.09 $\pm$ 00.02, 21.74 $\pm$ 00.01, 21.45 $\pm$ 00.02, 21.07 $\pm$ 00.03, 20.99 $\pm$ 00.09)
DES J2113–0114	318.484646	–1.240613	(22.51 $\pm$ 00.02, 20.97 $\pm$ 00.01, 20.28 $\pm$ 00.01, 19.89 $\pm$ 00.01, 19.99 $\pm$ 00.04)
A1	318.483975	–1.240611	(23.06 $\pm$ 00.04, 22.40 $\pm$ 00.03, 22.05 $\pm$ 00.03, 21.74 $\pm$ 00.04, 22.06 $\pm$ 00.28)
A2	318.484287	–1.240847	(21.60 $\pm$ 00.01, 21.07 $\pm$ 00.01, 20.67 $\pm$ 00.01, 20.42 $\pm$ 00.01, 20.72 $\pm$ 00.08)
DES J2321–4630	350.367937	–46.513625	(23.24 $\pm$ 00.05, 21.53 $\pm$ 00.02, 20.54 $\pm$ 00.01, 20.05 $\pm$ 00.01, 20.06 $\pm$ 00.03)
A1	350.369406	–46.514079	(23.26 $\pm$ 00.05, 22.45 $\pm$ 00.04, 21.75 $\pm$ 00.03, 21.26 $\pm$ 00.03, 21.26 $\pm$ 00.11)
A2	350.368353	–46.512958	(22.87 $\pm$ 00.03, 22.26 $\pm$ 00.03, 21.59 $\pm$ 00.03, 21.16 $\pm$ 00.03, 21.06 $\pm$ 00.08)
DES J2349–5113	357.375254	–51.227520	(22.01 $\pm$ 00.01, 19.91 $\pm$ 00.00, 19.28 $\pm$ 00.00, 18.91 $\pm$ 00.00, 18.78 $\pm$ 00.02)
A1*	357.374425	–51.228842	(23.43 $\pm$ 00.05, 22.69 $\pm$ 00.04, 22.40 $\pm$ 00.03, 21.94 $\pm$ 00.03, 21.56 $\pm$ 00.02)
A2	357.373730	–51.227069	(22.45 $\pm$ 00.02, 21.82 $\pm$ 00.02, 21.53 $\pm$ 00.02, 21.15 $\pm$ 00.02, 20.86 $\pm$ 00.12)

*Notes.* Positions and photometry of objects for each confirmed strong-lensing system. ‘Object name’ refers to each system (DES system name) or lensed source image (e.g. A1) discussed in the text, in Figs 1 and 2–10. All positions (RA, Dec. in J2000) and magnitudes (with Mag\_Auto derived from SOURCEEXTRACTOR) are drawn from the DESDM database, except for some source images that were too faint to detect or were blended with nearby objects in the automated data reduction process – these are marked by an asterisk \*. For these objects, we measured aperture magnitudes via the Graphical Astronomy and Image Analysis software tool (GAIA 2015). Also note that Mag\_Auto suffers from segmentation issues and so the magnitudes cannot be used for stellar mass estimates.

**Table 2.** Spectroscopic observation log.

DES system name	UT date	Grating	Integration time (h)	Seeing (arcsec)
DES J0041–4155	2015 Oct 11, 12	R400/B600	0.93/1.00	1.11/1.47
DES J0104–5341	2015 Oct 11	R400/B600	1.87/1.00	1.83/1.55
DES J0120–5143	2015 Oct 11	R400	1.00	1.42
DES J0227–4516	2015 Oct 8, 9	R400/B600	1.67/1.00	1.83/–
DES J0227–4516	2016 Dec 1, 5	R400/B600	1.00/1.00	0.73/0.63
DES J0357–4756	2015 Dec 8	R400/B600	0.93/1.	0.87/0.81
DES J0418–5457	2016 Dec 1, 3	R400/B600	1.00/1.00	0.8/0.85
DES J2113–0114	2015 Oct 11	R400	1.00	1.83
DES J2321–4630	2015 Oct 12	R400	1.00	1.3
DES J2349–5113	2015 Dec 7	R400	1.00	0.76

*Notes.* Observation log for follow-up spectroscopic observations. DES system name is derived from the RA and Dec. position of the lensing object at the centre of the system. The seeing is taken from the Gemini Observation Logs, which keep environmental conditions in 2-h increments: The seeing for each exposure set is the average of the seeing recorded at the time-steps in the Gemini environmental logs that bracket the observations of interest.

**Table 3.** Inconclusive and rejected candidates.

Object name	RA (J2000) ( $^{\circ}$ )	Dec. (J2000) ( $^{\circ}$ )	Confirmation status
DES J0205–4038	31.272	–40.642	Inconclusive
DES J0217–5245	34.309	–52.758	Rejected
DES J0300–5001	45.090	–50.025	Inconclusive
DES J0322–5234	50.567	–52.576	Inconclusive
DES J0342–5355	55.520	–53.921	Inconclusive
DES J0428–4409	67.081	–44.166	Rejected
DES J0450–5715	72.537	–57.256	Inconclusive
DES J0510–5637	77.555	–56.632	Inconclusive
DES J0536–5338	84.022	–53.647	Inconclusive
DES J0538–4735	84.518	–47.588	Inconclusive
DES J0602–4524	90.693	–45.412	Inconclusive
DES J2127–5149	321.779	–51.831	Inconclusive

*Notes.* A list of all systems that could not be confirmed as a strong-lensing system – either the data are ‘inconclusive’ for a confirmation or the data indicate that the system can be ‘rejected’. ‘Object name’ refers to each system (DES system name). All positions are shown in RA, Dec. in J2000. DES J0217–5245 was rejected: The source object appears to be a multiply imaged red galaxy, but this turned out to be a background group. DES J0428–4409 was also rejected: The blue source galaxy is actually a foreground star-forming galaxy were made?

objects, like lensed quasars and supernovae, to measure the Hubble rate, in a manner largely independent of dark matter and dark energy densities (Refsdal 1964; Blandford & Narayan 1992) or the dark energy equation of state (see Linder 2011). Recent work by the H0LiCOW ( $H_0$  Lenses in COSMOGRAIL’s Wellspring) collaboration provides constraints on the Hubble constant with a precision that is competitive with other standard cosmological probes (Suyu et al. 2017; Bonvin et al. 2017).

Lenses of different kinds have been the object of targeted searches in DES, including quasar lenses (Agnello et al. 2015, 2017; Lin et al. 2017; Ostrovski et al. 2017), as well as galaxy–galaxy lenses (Nord et al. 2016). The lensed quasar search is the focus of the STRong-lensing Insights into DES (STRIDES) programme.<sup>3</sup> The current work extends this line of DES-wide investigation, with galaxy–galaxy lenses spanning different environments: isolated galaxies, groups, and clusters. Spectroscopic confirmation is time-consuming, yet a critical process for astrophysical and cosmological analyses. While thousands of candidates may be observable with DES, the sample size that is optimized for the aforementioned science goals is constrained by observational resources and the number of systems with science potential.

In this work, we describe the spectroscopic confirmation of nine new strong-lensing systems discovered in DES Year 1 (Y1) data. We selected these systems based on the brightness of source galaxies, as well as on the potential for modelling the system – i.e. morphological simplicity and potential to examine the mass profile of the underlying dark matter halo. We first created lists of candidates based on (i) samples of galaxy groups and clusters, and (ii) photometrically selected galaxies – totaling  $\sim 9500$  candidates. We then visually inspected an image of each candidate system. This led to the selection of 46 candidates, and we performed a spectroscopic follow-up on 21 of those. We then analysed the spectroscopic data to determine the redshifts of the sources in those

lenses to discern if the systems are indeed strong lenses. We describe in more detail the lens candidate search process in Section 3.

In this work, we focus on nine systems (shown in Fig. 1) that show pieces of evidence – morphology, photometry, and spectroscopy – of strong gravitational lensing: Three of the systems are galaxy-scale lenses, five are group-scale lens, and one is a cluster-scale lens. All of them are newly discovered and confirmed objects. Detailed mass models of a subset of the confirmed systems will be presented in a separate paper (see Poh et al., in preparation).

This paper has the following structure. We describe the DES Y1 data in Section 2. We discuss the search for lens candidates in Section 3 and then the follow-up spectroscopic observations and analysis in Section 4. We present the nine confirmed systems and their properties in Section 5. We then conclude in Section 6. The AB system is used for all magnitudes. A Planck  $\Lambda$  cold dark matter ( $\Lambda$ CDM) cosmology with spatially flat priors is assumed:  $\Omega_M = 0.308$ ,  $\Omega_\Lambda = 0.692$ , and  $H_0 = 67.8 \text{ km s}^{-1} \text{ Mpc}^{-1}$  (see Planck Collaboration XIII 2015).

## 2 DES YEAR 1 DATA

DES covers  $\sim 5000 \text{ deg}^2$  in a deep, wide-field survey of the southern Galactic Cap in five optical filters ( $grizY$ ). It extends to a depth of  $i \sim 24$  mag at a  $10\sigma$  detection threshold and a  $27 \text{ deg}^2$  supernova survey across 10 fields – two deep and eight shallow. The depth in the repeated supernova area is typically two magnitudes deeper than the wide-field survey. The survey is undertaken with the Dark Energy Camera (DECam; Flaugher et al. 2015), which is a  $3 \text{ deg}^2$  CCD mosaic camera mounted on the BLANCO 4-m telescope at the Cerro Tololo Inter-American Observatory (CTIO) in the Chilean Andes. The DES footprint is observable between August and mid-February. Each year, DES is allocated  $\sim 105$  nights, and it has now completed all five-and-a-half years of planned observations. Because of its large field of view and red-sensitive CCDs, DECam is particularly suited to high-redshift survey work.

For this work, we use the Year One First Annual (Y1A1) internal collaboration release of the DES data. The survey and operations are described in Diehl et al. (2014). The data in the Y1A1 release were acquired between 2013 August 15 and 2014 February 9. These data cover  $\sim 1840 \text{ deg}^2$  to a median  $10\sigma$  point-source depth calculated with SOURCEEXTRACTOR’s fixed-aperture magnitudes (MAG APER), with 1.95-arcsec apertures, of 24.19, 23.85, 23.25, 22.55, and 21.20 in the  $g$ ,  $r$ ,  $i$ ,  $z$ , and  $Y$  bands, respectively (see Drlica-Wagner et al. 2018a).

The reduction of the images from DES Y1 data was performed by the DES data management (DESDM) team (see Morganson et al. 2018). After detrending, the single-epoch images were combined into ‘co-add tiles’ after first being calibrated and background-subtracted. The tiles are co-add images comprising one to five exposures in each of the five wavelength bandpasses. On average, in each tile, the coverage comprised 3.5 exposures. Each co-add tile has dimensions  $0.73 \times 0.73 \text{ deg}^2$ , which are defined to cover the full footprint of DES homogeneously. The final survey depth is deeper than the Y1A1 release, which consists of 3707 co-add tiles. This footprint covers two non-contiguous regions: One overlaps the deeply imaged Stripe 82 (see Jiang et al. 2014) from SDSS (see York et al. 2000; Abazajian et al. 2009) and the other overlaps the area that is covered by the South Pole Telescope (SPT; Carlstrom et al. 2011). More details of the reductions are available in Drlica-Wagner et al. (2018b).

The SOURCEEXTRACTOR (Bertin & Arnouts 1996; Bertin 2011) image detection software is used for catalogue source detection.

<sup>3</sup><http://strides.astro.ucla.edu/>

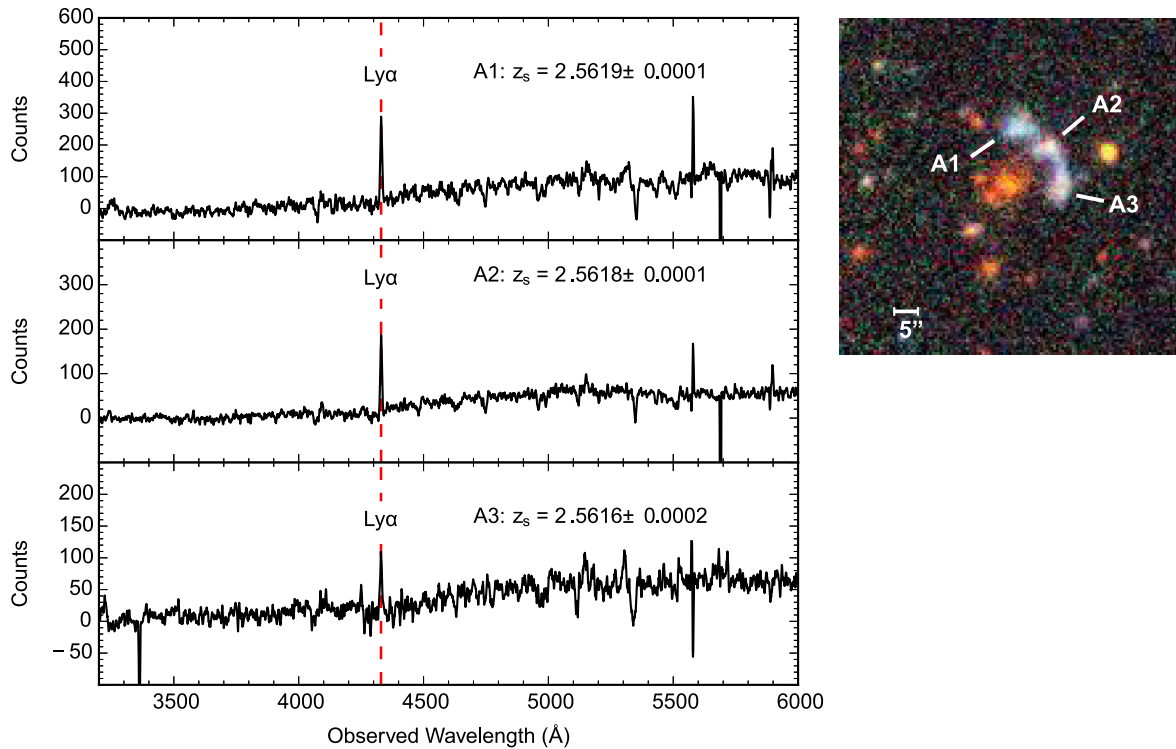


**Figure 2.** DES J0041–4155. The 1D spectra for A1, A2, and A3 are shown on the left-hand panels. There are emission lines near the same observed wavelength  $\sim 4329 \text{ \AA}$  in all three *B600* spectra. We assign these features to be Ly $\alpha$ , which gives redshifts of  $z_{\text{source}} = 2.5619 \pm 0.0001$ ,  $2.5618 \pm 0.0001$ , and  $2.5616 \pm 0.0002$  for A1, A2, and A3, respectively. The spectra are smoothed using a boxcar with a width of 5 pixels with the IRAF task *splot*. In the colour co-add image in the top right-hand panel, the three features of interest are labelled, and the scale bar shows the size of the image. In the lower right-hand panel is an identical colour co-add image. Both images are oriented north up, east left.

It is deployed in a double-image mode, and for the detection image, it uses the  $\chi^2$  detection image, which is constructed from the combination of the *r*-, *i*-, and *z*-band images. Positional and photometric data of all the objects in this study (see Table 1) come from this object catalogue. While MAG APER is used for the measures of depth in the Y1A1 catalogue release, in this work, we use the magnitude measure, Mag\_Auto, to perform catalogue searches for lens candidates.

### 3 LENS SEARCH

To identify candidates in DES Y1 data, we used (i) samples of galaxy clusters selected via DES data or via SPT data, and (ii) galaxies selected based on photometry. A number of expert scanners visually inspected candidates in search of visually compelling evidence (e.g. morphology, colour, brightness) that the systems would be useful for mass modelling.

The search method used to create candidate lists for visual inspection primarily selects for blue or red source galaxies near single galaxies or within groups or clusters of galaxies. Searches of 7328 optically selected galaxy clusters – found with the REDMAPPER algorithm (Rykoff et al. 2014) – as well as a selection of galaxies from the redMaGiC catalogue (Rozo et al. 2016; Cawthon et al. 2017) yielded 374 candidates in the DES Y1 footprint. This is described in section 3.3 of Diehl et al. (2017), which will from here on be referred to as *Diehl17*. A third search of SPT galaxy clusters yielded 66 more candidates (described in section 3.1 of *Diehl17*). Candidates from searches described elsewhere in *Diehl17* added 88

more. Some candidates were the result of serendipitous discovery, and those were not described in *Diehl17*.

The combined searches resulted in a list of 112 candidate systems. A sample of 46 candidates were selected on the bases of (i) science cases (e.g. the potential for modelling the dark matter halo of the lens itself), and (ii) objects that are already targeted by other follow-up efforts (e.g. some SPT clusters). Note that the ranking discussed in *Diehl17* is purely based on how likely an object is to be a lens (not on how easy it would be to follow up).

We cross-checked both our follow-up candidate sample and the full Y1A1 footprint against the Master Lens Database (MLDB; last updated 2018 February 2), which contains 674 candidates and confirmed systems. None of the candidates we observed during our follow-up for this paper is found in MLDB.

There are two areas in the DES Y1A1 footprint: one overlaps with SPT and the other overlaps with SDSS Stripe 82. From MLDB, 202 lenses are within the Y1A1 footprint – 28 in the SPT area and 174 in Stripe82 area. Those in the SPT area have sufficiently high redshift to not be visible within wavelengths observed by DES. Those in the Stripe82 area were already discovered and are not within our follow-up sample.

### 4 SPECTROSCOPIC FOLLOW-UP AT GEMINI/GMOS

In this paper, we aim to report the spectroscopic evidence for strong gravitational lensing in a sample of candidates that were selected through visual scans of images. We identified 46 candidates during the lens search, from which we chose the 21 candidates that are most

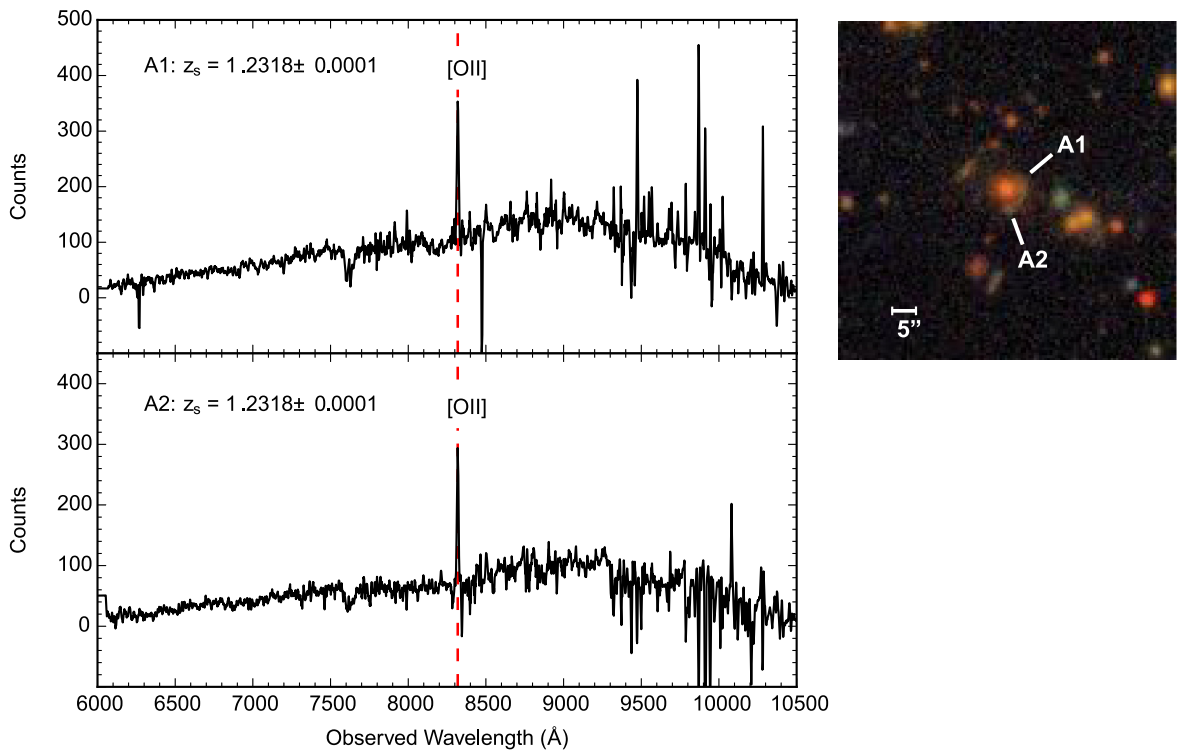


**Figure 3.** DES J0104–5341. The 1D spectra for source images A1 and A2 are shown on the left-hand panels. There are emission lines in both  $R400$  spectra near an observed wavelength of  $\sim 8319 \text{ \AA}$ . We associate this feature with [O II], which yields redshifts of  $z_{\text{source}} = 1.2318 \pm 0.0001$  and  $1.2318 \pm 0.0001$  in A1 and A2, respectively. The spectra are smoothed using a boxcar with a width of 5 pixels with the IRAF task `splot`. In the colour co-add image in the top right-hand panel, the two features of interest are labelled ‘A1’ and ‘A2’, and the scale bar shows the size of the image. In the lower right-hand panel is an identical colour co-add image. Both images are oriented north up, east left.

suitable for a follow-up with spectroscopic observations and analysis. The bases for this downselection are the (i) brightness of source galaxies, and (ii) suitability of system for observation (e.g. mask alignment). We measure the spectroscopic redshifts of source galaxies to determine if they are larger than the putative lens redshifts.

We require a wide spectral range to search for patterns of narrow emission lines. We expect some sources to be late-type emission-line galaxies. With these, we look for several features, such as [O III] and H $\beta$  to  $z \sim 1.0$ ; H $\delta$ , H $\gamma$ , and [O II]<sup>4</sup> to  $z \sim 1.7$ ; and Ly $\alpha$  in the range  $z \sim 2.7$ –7.2.

As part of the Gemini Large and Long Program (GS-2015B-LP-5 and GS-2016B-LP-5),<sup>5</sup> we used the multi-object mode of the Gemini Multi-Object Spectrograph (GMOS; Hook et al. 2004) at the Gemini South telescope for spectroscopic observations of our candidates. This proposal includes the goal of creating a spectroscopic sample of red galaxies for photometric redshift calibration. Below, we describe the observing strategy and the reductions of the spectroscopic data.

#### 4.1 Observing strategy

We used the following procedure for planning the follow-up. For the purposes of planning the follow-up, we first ranked 21 candidates by their  $i$ -band surface brightness, which is calculated using an

<sup>4</sup>Here, we refer to the doublet, because our resolution is not sufficient to resolve both lines in the doublet.

<sup>5</sup><http://www.gemini.edu/?q=node/12238#Buckley>

aperture that is 2 arcsec in diameter. We defined three sets of gratings and exposure times. The combinations depend on these surface brightness classes: For objects with surface brightness  $i_{\text{SB}} < 23$ , we integrate for 1 h in the  $R400$  grating; for objects with surface brightness  $23 < i_{\text{SB}} < 24$ , we integrate for 3.7 h in the  $R400$  grating and then for 1 h in the  $B600$  grating; for objects with surface brightness  $i_{\text{SB}} > 24$ , we integrate for 1 h in the  $B600$  grating. See Table 2 for details of the observations that were performed.

We mostly performed 1-h observations, which allowed us to obtain a sufficient signal in the cases for which a lens could be confirmed in that amount of time. More than 1 h of integration would be unlikely to yield an enough additional signal-to-noise ratio to warrant spending the time. In the event that a clear signal did not appear during the prescribed observations, we chose to not perform additional observations or longer integration times for any system. We made this decision to conserve telescope time and to maximize the number of strong-lens-system confirmations. Moreover, consistent integration times across the observation fields incur consistent depths – a requirement for the photo- $z$  calibration targets.

We centred each field’s mask on the lens of the candidate system, and we placed slits on the images of the sources. In some cases, we shifted the centre of the field to accommodate a suitable guide star. We also rotated the slit mask (i.e. rotated the position angle of the system) to include as many source targets as possible. Slits were first placed on as many of the source images as possible. Then, for the calibration of DES photometric redshifts, the unused slits (about 40) were placed on galaxy targets. While the slit lengths varied, all the slits were 1 arcsec in width. This setting accommodated both

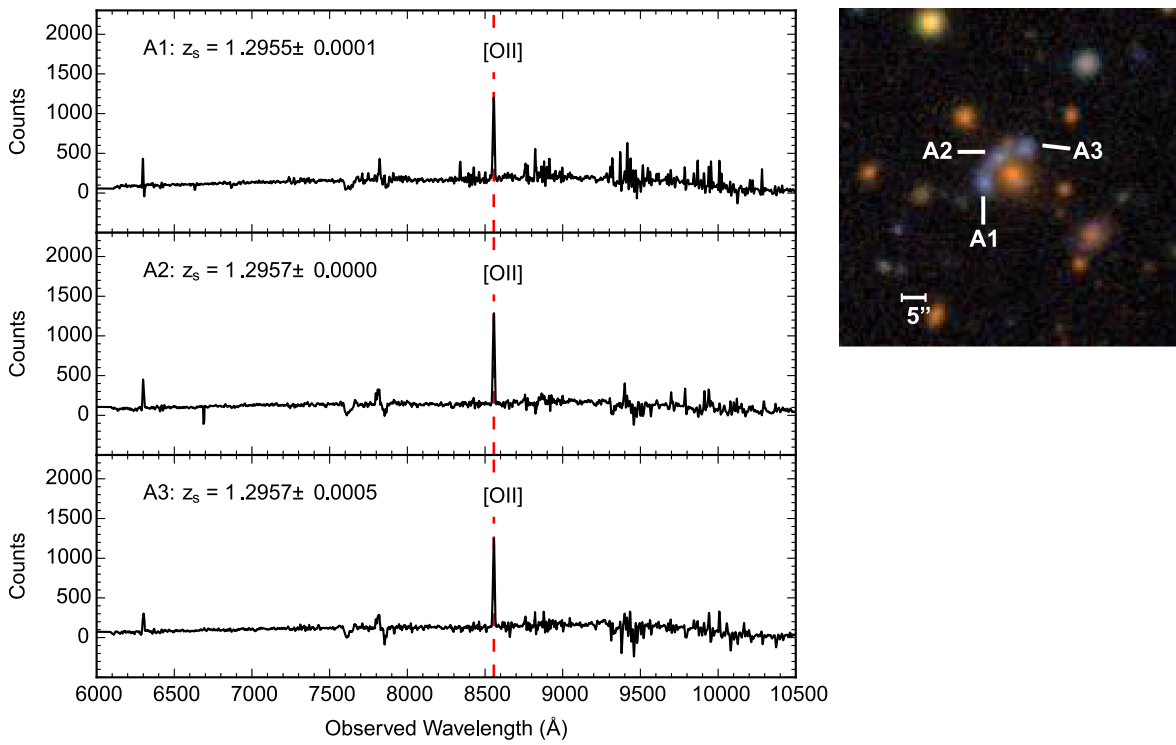


**Figure 4.** DES J0120–5143. The 1D spectra for source images A1, A2, and A3 are shown in the left-hand panels. There are emission lines in all three *R400* spectra near  $\sim 8556 \text{ \AA}$ , which we identify as [O II], and from which we obtain redshifts  $z_{\text{source}} = 1.2955 \pm 0.0001$ ,  $1.2957 \pm 0.0000$ , and  $1.2957 \pm 0.0005$  for A1, A2, and A3, respectively. The spectra are smoothed using a boxcar with a width of 5 pixels with the *IRAF* task *spplot*. In the colour co-add image in the top right-hand panel, the three features of interest are labelled ‘A1’, ‘A2’, and ‘A3’. The scale bar shows the size of the image. The image is oriented north up, east left.

the object and the amount of sky sufficient for reliable background subtraction. In some cases, the slits were tilted to maximize the flux captured from an extended source.

To obtain spectra of objects with redshift  $z < 1.7$  and wavelength coverage  $\sim 5000$ – $10\,000 \text{ \AA}$ , we use the *R400* grating in conjunction with the *GG455* filter. For spectra of objects with redshift  $z > 2$  and within the wavelength range  $3250$ – $6250 \text{ \AA}$ , we use the *B600* grating without a filter.

For an observing sequence with a 1-h science integration, we first took a pair of half-hour 900-s science exposures. Then, we used a Quartz-Halogen lamp to take a flat-field and a Quartz-Halogen lamp to take a calibration spectrum. To cover the gap between the CCDs, we then shifted to a different central wavelength. Finally, we repeated this sequence in reverse order. For the 3.7-h science integration, we instead used 840-s science exposures and repeated the above sequence 16 times. We facilitated the removal of cosmic rays by dividing the integration time into multiple exposures. We binned the data  $2 \times 2$ , which gave effective dispersions of  $1.0$  and  $1.5 \text{ \AA pixel}^{-1}$  for the *B600* and *R400* gratings, respectively.

## 4.2 Spectroscopic reductions

We used the Gemini *IRAF* package v1.13.1<sup>6</sup> for *IRAF* v2.16 to reduce the exposures. Some of the Gemini *IRAF* tasks were modified to provide additional flexibility in the data reduction. First, for each wavelength dither in a given system, we use the *gsflat* task to process (including bias subtraction) the flat-field. We then use

these processed flat images and *gsreduce* to reduce each science exposure. Then, the two exposures are combined with *gemcombine*. We then use the *gswavelength* and *gsttransform* tasks to perform wavelength calibration and transformation on each dither.

Then, we co-add a pair of dithers on the new common wavelength scale, which eliminates CCD chip gaps. We use *gsextract* (which calls the *apall* task) to perform sky subtraction and one-dimensional (1D) spectral extraction. We use night sky lines from the science spectra to add calibration lines to the  $5500$ – $6400 \text{ \AA}$  wavelength range. We modified the canonical reduction process by taking the log of the fluxes in the calibration spectra to enable simultaneous automated identification of both the strong lines above  $7000 \text{ \AA}$  and the weaker lines below that. For improved interactive flexibility in this part of the reduction, *gswavelength* and *gsextract* were modified to allow wavelength calibration and 1D spectral extraction, respectively, for selected individual slits, as needed. Finally, we use the *emsao* task within the *rvsao* *IRAF* package (Kurtz & Mink 1998) for feature identification and redshift estimation.

## 5 SAMPLE OF CONFIRMED LENSES

We confirmed that 9 of the 21 observed candidate systems are indeed strong-lensing systems, and we rejected two candidates. The remaining 10 were not confirmed, and spectroscopic analysis was inconclusive for those candidates.

One of the two rejected systems contains a foreground star-forming galaxy, and the other contains a background group (rather

<sup>6</sup><http://www.gemini.edu/sciops/data-and-results/processing-software>

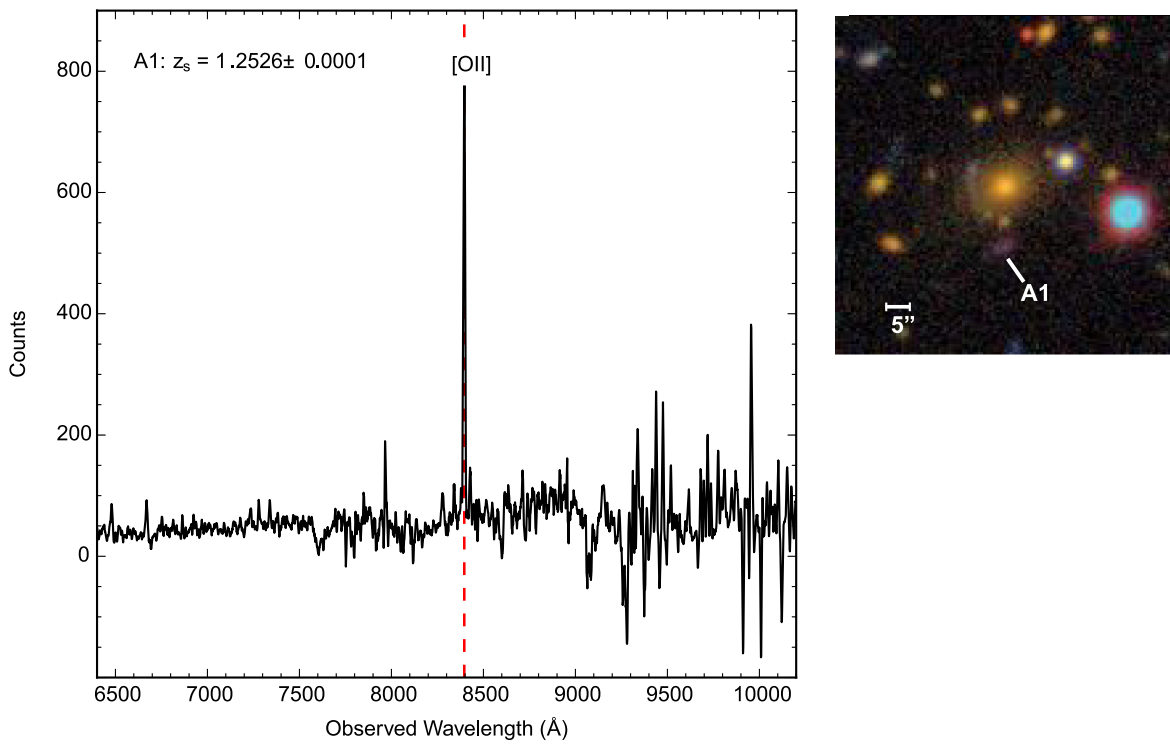


**Figure 5.** DES J0227–4516. The 1D  $R400$  spectrum for A1 is shown in the left-hand panel. The prominent emission lines near observed wavelengths  $\sim 8396 \text{ \AA}$  are considered to be [O II]. These lines yield source spectroscopic redshifts of  $z_{\text{source}} = 1.25264 \pm 0.00009$  for A1. The spectra are smoothed using a boxcar with a width of 5 pixels with the IRAF task `splot`. In the colour co-add image in the right-hand panel, the feature of interest is labelled ‘A1’. The scale bar shows the size of the image. The image is oriented north up, east left.

than the apparent multiply lensed red galaxy). The systems that we failed to confirm exhibit promising lensing features, but the sources have no discernible continuum emission, no spectral features, or both. The measurements of spectroscopic features are too low signal-to-noise ratios with the integration times in our observing programme, or they have redshifts that are outside the range of the optical observations in our observing programme (i.e. in the redshift desert). We list the rejected and inconclusive systems in Table 3.

In Fig. 1, we show a multipanel figure of the confirmed systems. In Table 1, for each observed lensing system, we list the positions and photometry of the candidate lens and source(s). The sample is composed of three galaxy-scale lenses (b, f, g), five group-scale lenses (a, c, d, h, i), and one cluster-scale lens (e).

In this section, we provide details of each system – the important spectral features, the measured redshifts, and simple mass estimates. Figs 2–10 show the reduced 1D spectra and a cut-out of the field centred on the central lensing object, including labelled source positions for each system.

We estimate the enclosed mass  $M_{\text{enc}}$  of the lensing system under the assumption of a singular isothermal sphere mass profile (Narayan & Bartelmann 1996):

$$M_{\text{enc}} = \frac{c^2}{4G} \theta_e^2 \left( \frac{D_L D_S}{D_{LS}} \right), \quad (1)$$

where  $c$  is the speed of light,  $G$  is Newton’s gravitational constant,  $\theta_e$  is the Einstein radius, and  $D$  is the angular diameter distance. In particular,  $D_L$ ,  $D_S$ , and  $D_{LS}$  are the angular diameter distances to the lens, to the source, and between the lens and the source, respectively. We use the source image–lens separation (calculated in Diehl17) as an approximation for the Einstein radius  $\theta_{\text{sep}}$ . It is

measured by taking the average of the distances between a targeted source image and the selected central lensing galaxy. This estimate of the Einstein radius is only accurate to a factor of 2, and it is an overestimate for cases in which only the brightest source image is used to approximate the radius.

We use the standard deviation of the distances summed in quadrature with the pixel scale of DECam ( $0.263 \text{ arcsec pixel}^{-1}$ ) to estimate the uncertainty in this distance. The angular diameter distances depend only on redshifts of the objects and on cosmological parameters. Table 4 summarizes key information for all the confirmed systems – spectral features, photometric redshifts of lenses, spectroscopic redshifts of sources, source image–lens separation, and enclosed masses. This strategy is similar to that used in the Sloan Bright Arc Survey (SBAS; e.g. Diehl et al. 2009).

We combine uncertainties from the measurements of the distances and source image–lens separation to estimate frequentist uncertainties for the enclosed mass. According to the prescription of Sánchez et al. (2014) for photometric redshifts in DES, the photometric redshift uncertainties have been multiplied by a factor of 1.5. The spectroscopic redshift uncertainties are the result of a sum in quadrature of (i) the uncertainty in wavelength calibration, and (ii) the uncertainty in the redshift determination from the IRAF function `emsao`. These spectroscopic redshift uncertainties are then propagated to the angular diameter distances.

The mass uncertainty results from the sum in quadrature of uncertainties from the source image–lens separation, and the angular diameter distances. The uncertainty on each angular diameter distance scales with the redshift error, which falls in the range of  $\sim 0.008\text{--}0.19$  per cent for spectroscopic redshifts and  $\sim 3.2\text{--}17.5$  per cent for lens redshifts. The uncertainty in the source

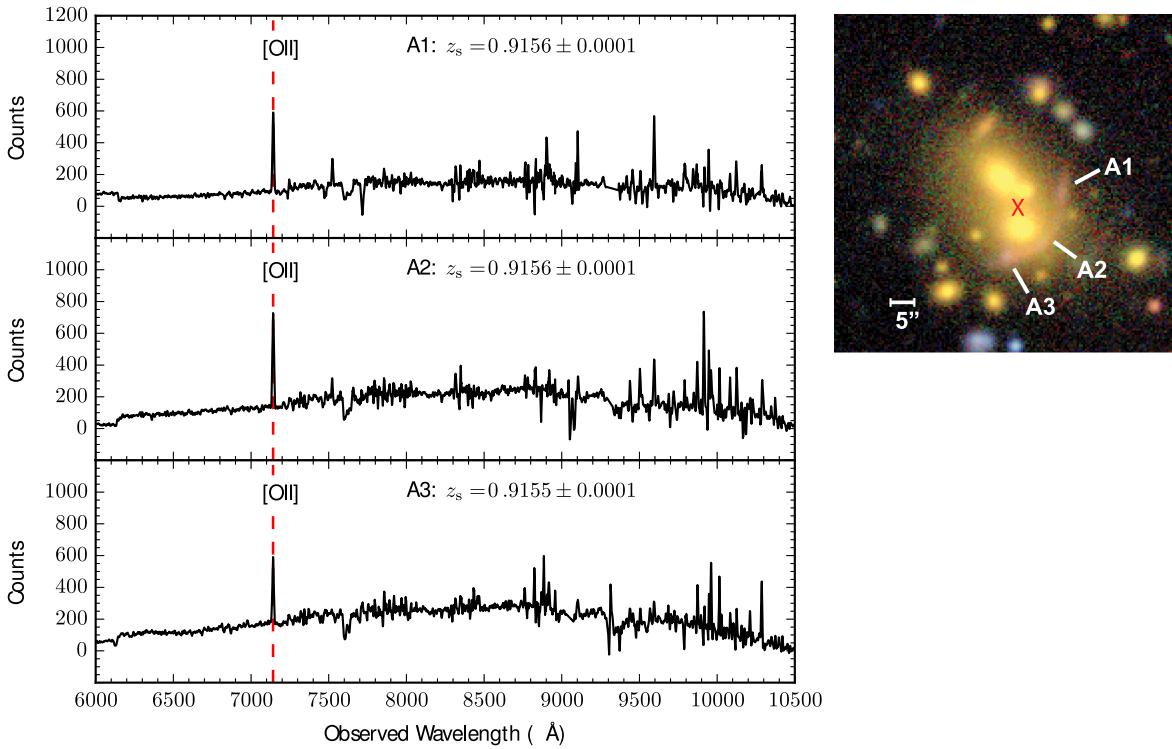


**Figure 6.** DES J0357–4756. The 1D spectra for source images A1, A2, and A3 are shown in the left-hand panels. Near the observed wavelength of  $\sim 7142$  Å, we identify [O II] in all three *R400* spectra, from which we obtain redshifts of  $z_{\text{source}} = 0.9156 \pm 0.0001$ ,  $0.9156 \pm 0.0001$ , and  $0.9155 \pm 0.0001$ , for A1, A2, and A3, respectively, and which are labelled in the colour co-add image in the top right-hand panel, along with a scale bar to show the size of the image. The spectra are smoothed using a boxcar with a width of 5 pixels with the IRAF task *splot*. The image is oriented north up, east left. The red ‘x’ near the centre of the colour image in the upper right-hand panel marks the position designated for the measurement of the Einstein radius. The position of the red ‘x’ is chosen to simplify the drawing of a circle through the arcs of the source galaxy images to extract the Einstein radius and lens mass.

image–lens separation, which falls in the range of  $\sim 6$ –22 per cent, is purely statistical. This results in mass uncertainties in the range of  $\sim 25$ –80 per cent. Table 4 summarizes the lensing features for the confirmed systems.

A subset of the systems have sources with multiple, detailed images, making them amenable to detailed modelling, which will be performed in a separate paper (Poh et al., in preparation).

### 5.1 DES J0041–4155

DES J0041–4155 is a group-scale system. The largest central red galaxy has a DESDM photometric redshift of  $z_{\text{lens}} = 0.7160 \pm 0.0310$ . As shown in Fig. 1(a), there are three prominent blue-pink arcs, A1, A2, and A3, to the north, north-west, and west, respectively, of the lensing galaxy. The right-hand panel of Fig. 2 also displays these arcs. We identify emission lines in the follow-up *B600* spectroscopy of the three images near the observed wavelength of  $\sim 4329$  Å in all three spectra (Fig. 2, left-hand panel). When we account for the absence of spectral features in the *R400* spectra, as well as the photometric redshift of the lens galaxy, we can assign spectral features to be Ly $\alpha$ . This then gives redshifts  $z_{\text{source}} = 2.5619 \pm 0.0001$ ,  $2.5618 \pm 0.0001$ , and  $2.5616 \pm 0.0002$  for A1, A2, and A3, respectively.

We identified no counter-images. In the *R400* spectrum for A1, there is an [O II] line at  $\sim 6620$  Å (not shown in Fig. 2), which corresponds to a redshift of  $z = 0.7761 \pm 0.00007$  of a foreground object. This is clearly visible as a bluer galaxy superimposed on A1.

We use the REDMAPPER redshift  $z_{\text{lens}} = 0.7317 \pm 0.0198$  and the estimated source image–lens separation of  $\theta_{\text{sep}} = 7.23 \pm 0.50$  arcsec

to calculate an enclosed mass of  $M_{\text{enc}} = (1.74 \pm 0.47) \times 10^{13} M_{\odot}$  for this system.

### 5.2 DES J0104–5341

DES J0104–5341 is a galaxy-scale lensing system. The red lensing galaxy has a photometric redshift  $z_{\text{lens}} = 0.6790 \pm 0.0220$ , and there are two relatively red arcs to the west and south, labelled A1 and A2, respectively, as shown in Fig. 1(b) and Fig. 3. We identify strong emission lines for A1 and A2 (Fig. 3, left-hand panel) in both *R400* spectra near an observed wavelength of  $\sim 8319$  Å. In the absence of features in the *B600* spectra, we associate this feature with [O II], yielding redshifts  $z_{\text{source}} = 1.2318 \pm 0.0001$  and  $1.2318 \pm 0.0001$  for A1 and A2, respectively. We see no counter-images for this source.

We use the REDMAPPER redshift  $z_{\text{lens}} = 0.6500 \pm 0.0259$  and the estimated source image–lens separation of  $\theta_{\text{sep}} = 2.18 \pm 0.43$  arcsec to calculate an enclosed mass of  $M_{\text{enc}} = (2.42 \pm 1.10) \times 10^{12} M_{\odot}$  for this system.

### 5.3 DES J0120–5143

The central red galaxy of this group-scale system, DES J0120–5143, has a photometric redshift  $z_{\text{lens}} = 0.6030 \pm 0.0630$ . There exist three source images, A1, A2, and A3, to the east, north-east, and north–north-west, respectively, of the central red galaxy in the image, as shown in Fig. 1(c) and in the right-hand panel of Fig. 4. In all *R400* data (Fig. 4, left-hand panel), there

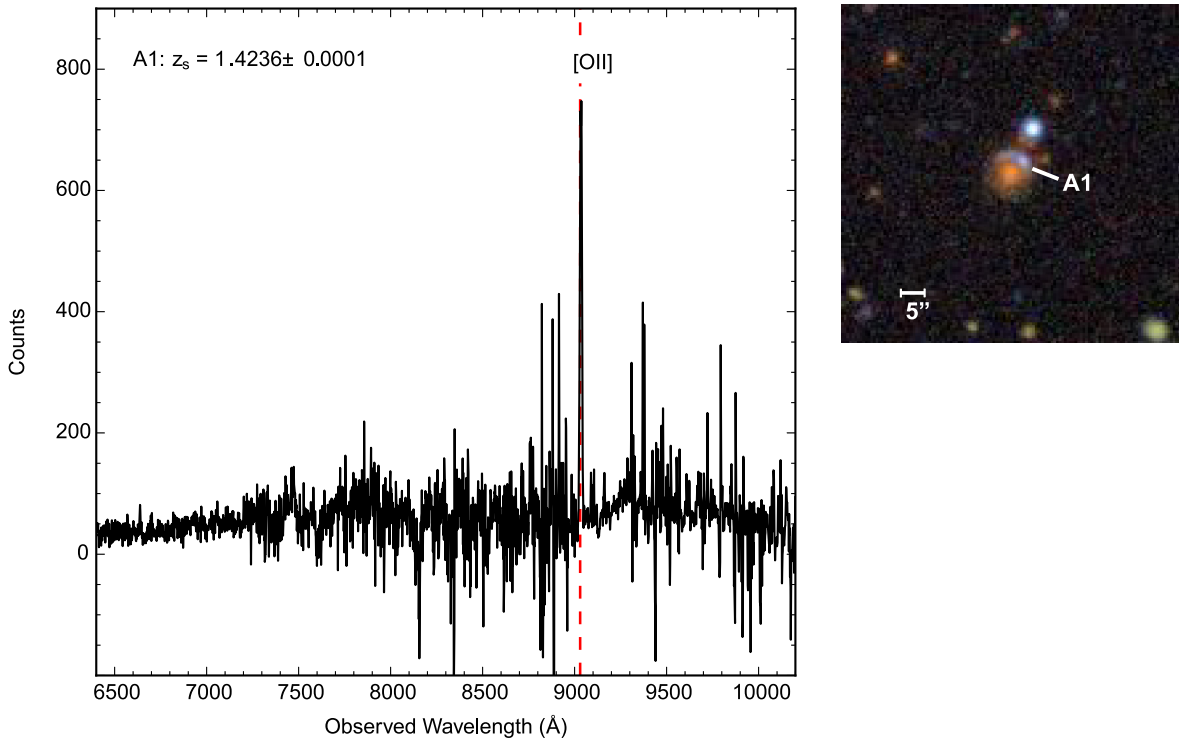


**Figure 7.** DES J0418–5457. The 1D  $R400$  spectrum for A1 is shown in the left-hand panel. The prominent emission lines near observed wavelengths  $\sim 8920$  Å are considered to be  $[O\text{ II}]$ . These lines yield source spectroscopic redshifts  $z_{\text{source}} = 1.4236 \pm 0.0001$  for A1. The spectra are smoothed using a boxcar with a width of 5 pixels with the IRAF task `splot`. In the colour co-add image in the top right-hand panel, the feature of interest is labelled ‘A1’. The scale bar shows the size of the image. The image is oriented north up, east left.

are emission-line features near  $\sim 8557$  Å, which we attribute to  $[O\text{ II}]$ . The resulting redshifts for the source images are  $z_{\text{source}} = 1.2955 \pm 0.0001$ ,  $1.2957 \pm 0.0000$ , and  $1.2957 \pm 0.0005$  for arcs A1, A2, and A3, respectively.

This lensing system resides in a group environment. There is a counter-image at the south-west that lies nearly on top of the central red lensing galaxy. We were not able to target it for follow-up spectroscopic observations.

We use the REDMAPPER redshift  $z_{\text{lens}} = 0.5238 \pm 0.0173$  and the estimated source image–lens separation of  $\theta_{\text{sep}} = 3.35 \pm 0.51$  arcsec to calculate an enclosed mass of  $M_{\text{enc}} = (4.46 \pm 2.78) \times 10^{12} M_{\odot}$  for this system.

#### 5.4 DES J0227–4516

DES J0227–4516 is a group-scale lens with the DES photometric redshift  $z_{\text{lens}} = 0.4300 \pm 0.0400$  and one blue knot (A1) to the south. The system is shown in Fig. 1(i) and in the right-hand panel of Fig. 5. Near wavelengths  $\sim 8396$  Å, we identify an  $[O\text{ II}]$  emission line in the  $R400$  spectra of the blue knot. This yields source redshifts of  $z_{\text{source}} = 1.25264 \pm 0.00009$  (A1) (Fig. 5, left-hand panel). We used the data from 2016 December to do the redshift determination, because the seeing was much better. We also targeted the faint arc to the east, but the signal-to-noise ratio of the data was too low, and we could not obtain a redshift.

We use the REDMAPPER redshift  $z_{\text{lens}} = 0.4347 \pm 0.0183$  and the estimated source image–lens separation of  $\theta_{\text{sep}} = 4.11 \pm 0.28$  arcsec to calculate an enclosed mass of  $M_{\text{enc}} = (4.32 \pm 1.32) \times 10^{12} M_{\odot}$  for this system.

#### 5.5 DES J0357–4756

DES J0357–4756 is a cluster-scale lens, where the central lensing galaxy has a photometric redshift  $z_{\text{lens}} = 0.2570 \pm 0.0240$ . There is a red arc (A1) to the west, a large red arc (A2) to the south-west, and a red arc (A3) to the south, respectively, as shown in Fig. 1(d) and in the right-hand panel of Fig. 6. In the follow-up  $R400$  spectroscopy of all three arcs (Fig. 6, left-hand panels), we identify an emission line at  $\sim 7141$  Å, which we identify as  $[O\text{ II}]$ . From this emission line, we obtain redshifts of  $z_{\text{source}} = 0.9156 \pm 0.0001$ ,  $0.9156 \pm 0.0001$ , and  $0.9155 \pm 0.0001$  (Fig. 6).

The red ‘x’ near the centre of the colour image in the upper right-hand panel marks the location of the lens designated for the measurement of the Einstein radius. The position of the red ‘x’ is chosen to simplify the drawing of a circle through the arcs of the source galaxy images. Because the goal is to obtain a simple estimate of the lens mass, our goal is to first obtain a reasonable estimate of the Einstein radius.

We use the REDMAPPER redshift  $z_{\text{lens}} = 0.2755 \pm 0.0129$  and the estimated source image–lens separation of  $\theta_{\text{sep}} = 9.39 \pm 0.91$  arcsec to calculate an enclosed mass of  $M_{\text{enc}} = (1.38 \pm 0.36) \times 10^{13} M_{\odot}$  for this system.

#### 5.6 DES J0418–5457

DES J0418–5457 is a galaxy-scale lens with the DES photometric redshift  $z_{\text{lens}} = 0.6130 \pm 0.0430$  and one blue arc (A1) to the north. The system is shown in Fig. 1(h) and in the right-hand panel of Fig. 7. Near a wavelength of  $\sim 9030$  Å, we identify an  $[O\text{ II}]$  emission line in the  $R400$  spectra of both arcs. This yields a

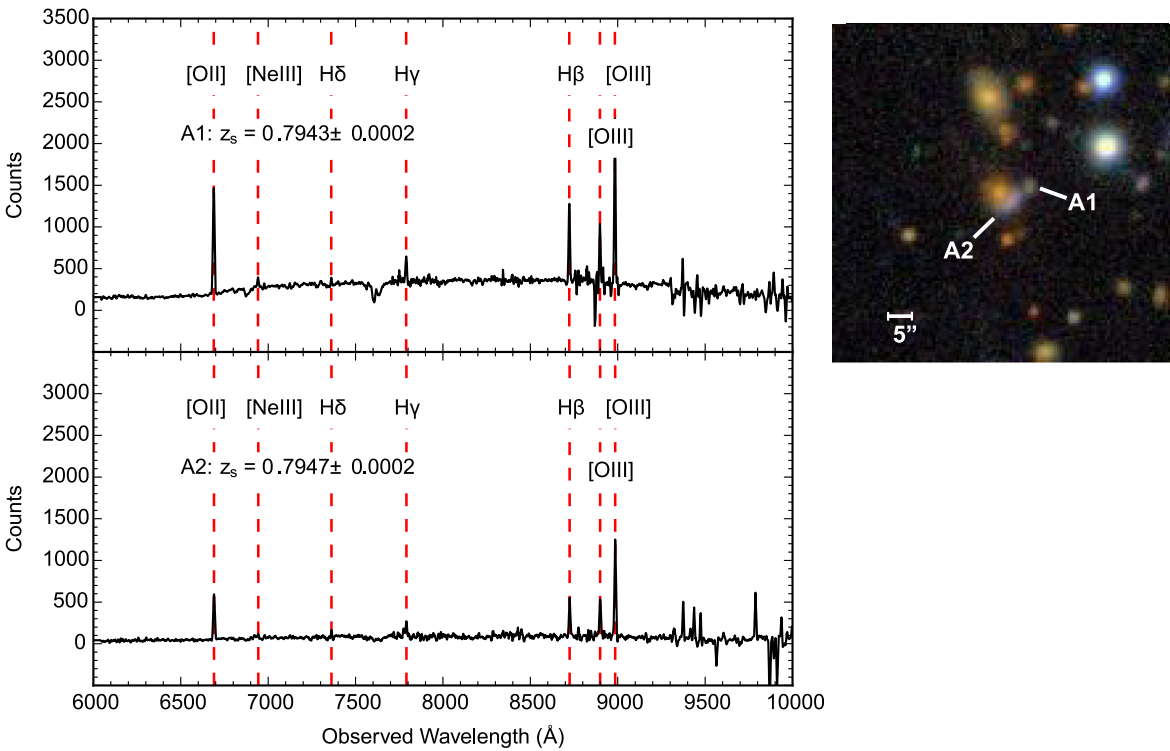


**Figure 8.** DES J2113–0114. The 1D  $R400$  spectra for source images A1 and A2 are shown in the left-hand panels. A1 presents emission lines near observed wavelengths of  $\sim 6689$ ,  $\sim 6942$ ,  $\sim 7790$ ,  $\sim 8723$ ,  $\sim 8898$ , and  $\sim 8984$  Å, which we conclude correspond to [O II], [Ne III] 3869, H $\delta$ , H $\gamma$ , H $\beta$ , [O III] 4959, and [O III] 5006, respectively. From these emission lines, we obtain redshifts of  $z_{\text{source}} = 0.7943 \pm 0.0002$  for A1 and  $0.7947 \pm 0.0002$  for A2. The spectra are smoothed using a boxcar with a width of 5 pixels with the IRAF task `splot`. In the colour coadded image in the top right-hand panel, the two features of interest are labelled ‘A1’ and ‘A2’, along with a scale bar to show the size of the image. The image is oriented north up, east left.

source redshift of  $z_{\text{source}} = 1.4236 \pm 0.0001$  (A1) (Fig. 7, left-hand panel).

We use the REDMAGiC redshift  $z_{\text{lens}} = 0.6130 \pm 0.0430$  and the estimated source image–lens separation of  $\theta_{\text{sep}} = 1.97 \pm 0.27$  arcsec to calculate an enclosed mass of  $M_{\text{enc}} = (1.47 \pm 0.65) \times 10^{12} M_{\odot}$  for this system.

## 5.7 DES J2113–0114

DES J2113–0114 is a galaxy-scale system with two small source images, A1 and A2, which lie to the south-west of the central red galaxy, as shown in Fig. 1(e) and in the right-hand panel of Fig. 8. The lensing galaxy has a photometric redshift  $z_{\text{lens}} = 0.4060 \pm 0.0710$ . In the  $R400$  spectra for A1, we identify emission-line features near  $\sim 6689$ ,  $\sim 6942$ ,  $\sim 7361$ ,  $\sim 7790$ ,  $\sim 8723$ ,  $\sim 8898$ , and  $\sim 8984$  Å. In both images, we take these emission lines to be [O II], [Ne III] 3869, H $\delta$ , H $\gamma$ , H $\beta$ , [O III] 4959, and [O III] 5006, respectively, from which we obtain redshifts of  $z_{\text{source}} = 0.7943 \pm 0.0002$  and  $0.7947 \pm 0.0002$  (Fig. 8) for these source images.

We use the REDMAGiC redshift  $z_{\text{lens}} = 0.4472 \pm 0.0187$  and the estimated source image–lens separation of  $\theta_{\text{sep}} = 1.98 \pm 0.51$  arcsec to calculate an enclosed mass of  $M_{\text{enc}} = (1.28 \pm 1.06) \times 10^{12} M_{\odot}$  for this system.

## 5.8 DES J2321–4630

DES J2321–4630 is a group-scale lens with two central galaxies with DESDM photometric redshifts  $z_{\text{lens}} = 0.6440 \pm 0.0250$  and  $0.70 \pm 0.02$ . There are two small red arcs, A1 and A2, to the east and

north-east, respectively, of the central red galaxy. These are shown in Fig. 1(f) and in the right-hand panel of Fig. 9. The  $R400$  spectrum of A1 shows prominent emission lines near five different observed wavelengths:  $\sim 6385$ ,  $\sim 6658$ ,  $\sim 9413$ , and  $\sim 10242$  Å, which we identify as C III] 2326, [Ne IV] 2424, [Ne V] 3346, and [O II], respectively. This gives a redshift of  $z_{\text{source}} = 1.7469 \pm 0.0014$ . The  $R400$  spectrum of A2 presents a similar pattern for these emission lines:  $\sim 6391$ ,  $\sim 6661$ ,  $\sim 9413$ , and  $\sim 10242$  Å, which yields a source redshift of  $z_{\text{source}} = 1.7479 \pm 0.0031$  (Fig. 9, left-hand panel). There is a possible counter-image to the south-southwest of the lensing galaxy, but it could not be targeted due to its proximity to the central red galaxy and available telescope time.

The presence of the Ne emission lines in combination with O II lines suggests the possibility that the source is a radio galaxy. Humphrey et al. (2007) identifies Ne V and Ne IV emission in  $z \sim 2.5$  radio galaxies as a potential signature of active galactic nucleus photoionization.

The two central galaxies are found in the REDMAGiC catalogue with redshifts  $z_{\text{lens}} = 0.6244 \pm 0.0240$  and  $0.6244 \pm 0.0240$ . We use the REDMAGiC redshifts and the estimated source image–lens separation of  $\theta_{\text{sep}} = 3.30 \pm 0.74$  arcsec to calculate an enclosed mass of  $M_{\text{enc}} = (3.84 \pm 1.87) \times 10^{12} M_{\odot}$  for this system.

## 5.9 DES J2349–5113

DES J2349–5113 is a group-scale lens. The central galaxy has a photometric redshift  $z_{\text{lens}} = 0.3450 \pm 0.0320$ , and there are two blue arcs (A1 and A2) to the east and the west. These are shown in Fig. 1(g) and in the right-hand panel of Fig. 10. Near wavelengths of  $\sim 8920$  Å, we identify [O II] emission lines in the  $R400$  spectra of

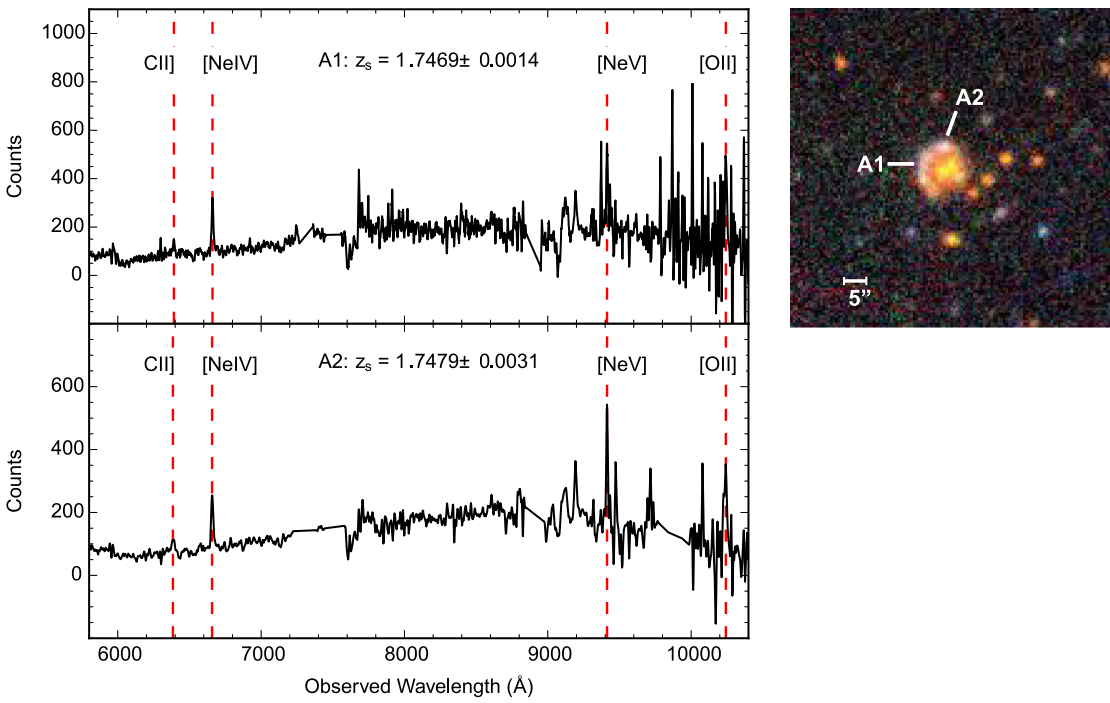


**Figure 9.** DES J2321–4630. The 1D  $R400$  spectra for sources A1 and A2 are shown in the left-hand panels. The emission lines at four different observed wavelengths in A1 at  $\sim 6385$ ,  $\sim 6658$ ,  $\sim 9413$ , and  $\sim 10\,242 \text{ \AA}$  are due to  $\text{C II}]$  2326,  $[\text{Ne IV}]$  2424, and  $[\text{O II}]$ , respectively. A similar pattern of emission lines occurs in A2 at  $\sim 6391$ ,  $\sim 6661$ ,  $\sim 9413$ , and  $\sim 10\,242 \text{ \AA}$ . These lines yield source spectroscopic redshifts of  $z_{\text{source}} = 1.7469 \pm 0.0014$  and  $1.7479 \pm 0.0031$  for A1 and A2, respectively. The spectra are smoothed using a boxcar with a width of 5 pixels with the IRAF task `splot`. In the colour coadded image in the top right-hand panel, the two features of interest are labelled ‘A1’ and ‘A2’. The scale bar shows the size of the image. The image is oriented north up, east left.

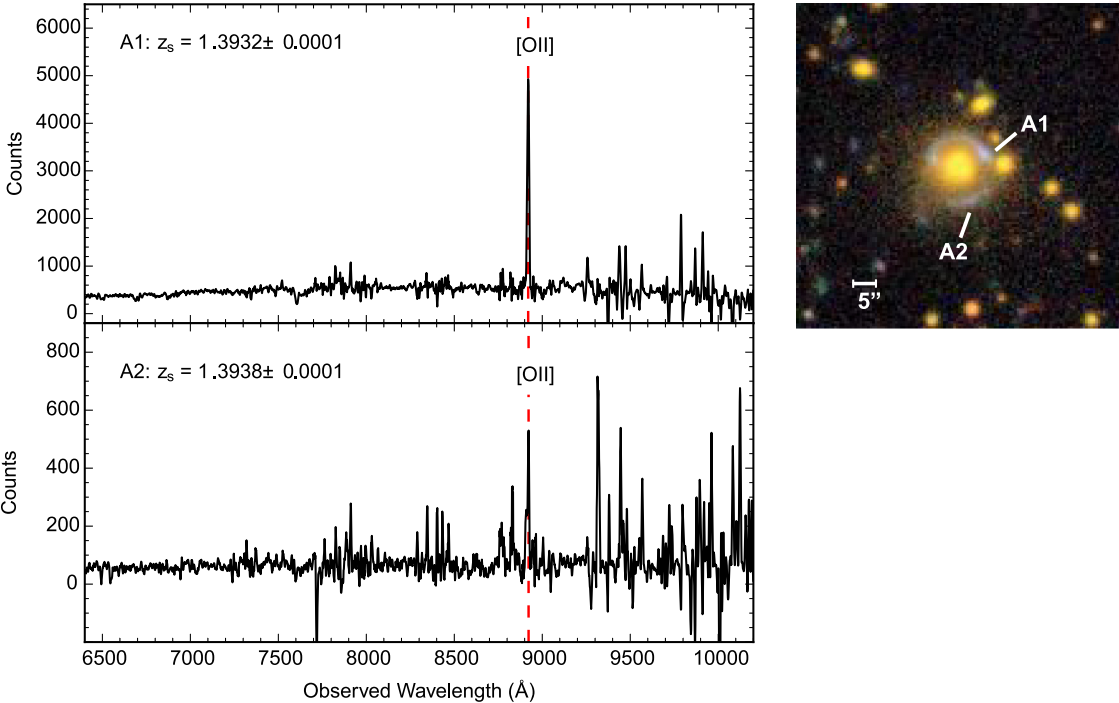


**Figure 10.** DES J2349–5113. The 1D  $R400$  spectra for A1 and A2 are shown in the left-hand panels. The prominent emission lines near observed wavelengths  $\sim 8920 \text{ \AA}$  are considered to be  $[\text{O II}]$ . These lines yield source spectroscopic redshifts of  $z_{\text{source}} = 1.3932 \pm 0.0001$  and  $1.3938 \pm 0.0001$  for A1 and A2, respectively. The spectra are smoothed using a boxcar with a width of 5 pixels with the IRAF task `splot`. In the colour coadded image in the top right-hand panel, the two features of interest are labelled ‘A1’ and ‘A2’. The scale bar shows the size of the image. The image is oriented north up, east left.

**Table 4.** Lensing features.

Object name	Spectral features	Redshift $z_{\text{lens}}$ OR $z_{\text{source}}$	Separation $\theta_{\text{sep}}$ (arcsec)	Enclosed mass $M_{\text{enc}}$ ( $M_{\odot}$ )
DES J0041–4155	...	0.7317 ± 0.0198	...	...
A1	Ly $\alpha$	2.5619 ± 0.0001	7.2 ± 0.5	(1.7 ± 0.5) × 10 <sup>13</sup>
A2	Ly $\alpha$	2.5618 ± 0.0001	...	...
A3	Ly $\alpha$	2.5616 ± 0.0002	...	...
DES J0104–5341	...	0.6500 ± 0.0259	...	...
A1	[O II]	1.2318 ± 0.0001	2.2 ± 0.4	(2.4 ± 1.1) × 10 <sup>12</sup>
A2	[O II]	1.2318 ± 0.0001	...	...
DES J0120–5143	...	0.5238 ± 0.0173	...	...
A1	[O II]	1.2955 ± 0.0001	3.4 ± 0.5	(4.5 ± 2.8) × 10 <sup>12</sup>
A2	[O II]	1.2957 ± 0.0000	...	...
A3	[O II]	1.2957 ± 0.0005	...	...
DES J0227–4516	–	0.4347 ± 0.0183	...	...
A1	[O II]	1.2526 ± 0.0001	4.1 ± 0.3	(4.3 ± 1.3) × 10 <sup>12</sup>
DES J0357–4756	–	0.2755 ± 0.0129	...	...
A1	[O II]	0.9156 ± 0.0001	9.4 ± 0.9	(1.4 ± 0.4) × 10 <sup>13</sup>
A2	[O II]	0.9156 ± 0.0001	...	...
A3	[O II]	0.9155 ± 0.0001	...	...
DES J0418–5457	–	0.6130 ± 0.0430	...	...
A1	[O II]	1.4236 ± 0.0001	2.0 ± 0.3	(1.5 ± 0.7) × 10 <sup>12</sup>
DES J2113–0114	–	0.4472 ± 0.0187	...	...
A1	[O II], [Ne III] 3868, H $\delta$ , H $\gamma$ , H $\beta$ , [O III] 4959, [O III] 5007	0.7943 ± 0.0002	2.0 ± 0.5	(1.3 ± 1.1) × 10 <sup>12</sup>
A2	[O II], [Ne III] 3868, H $\delta$ , H $\gamma$ , H $\beta$ , [O III] 4959, [O III] 5007	0.7947 ± 0.0002	...	...
DES J2321–4630	...	0.6427 ± 0.0363	...	...
A1	C II] 2326, [Ne IV] 2424, [Ne V] 3346, [O II]	1.7469 ± 0.0014	3.3 ± 0.7	(3.8 ± 1.9) × 10 <sup>12</sup>
A2	C II] 2326, [Ne IV] 2424, [Ne V] 3346, [O II]	1.7479 ± 0.0031	...	...
DES J2349–5113	...	0.4094 ± 0.0189	...	...
A1	[O II]	1.3932 ± 0.0001	4.5 ± 0.7	(3.8 ± 1.4) × 10 <sup>12</sup>
A2	[O II]	1.3938 ± 0.0001	...	...

*Notes.* Lensing features of confirmed systems. We show object names for lenses (DES system name) and image labels for sources (e.g. A1), names of spectral features, photometric redshifts of lenses  $z_{\text{lens}}$ , spectroscopic redshifts of sources  $z_{\text{source}}$ , an Einstein radius  $\theta_e$  for each system, and the resulting enclosed masses  $M_{\text{enc}}$ . The principal spectral features are all emission lines. Redshifts for the lenses are the photometric redshifts drawn from the DESDM database, and they are the first redshifts listed for each system: The uncertainties have been multiplied by 1.5 times the original estimate, according to the results of Sánchez et al. (2014), for estimating uncertainties in DES photometric redshift measurement codes. Redshifts of the sources are those measured from a spectroscopic follow-up at Gemini South. All the redshifts for a given system are within sufficient agreement that we measure the enclosed masses using only the spectroscopic redshift of the first source and the source image–lens separation for the system. Instead of providing Einstein radii (see Poh et al., in preparation), here we provide rough estimates of the size of lensed features, computed as the weighted average of image-to-lens separation.

both arcs. These yield source redshifts of  $z_{\text{source}} = 1.3932 \pm 0.0001$  and  $1.3938 \pm 0.0001$  for A1 and A2, respectively (Fig. 10, left-hand panel). Only after sky subtraction was the line in A2 revealed. Note that A2 appears more extended and much fainter than A1, and, thus, has a much lower signal-to-noise ratio. The faintness of the source, along with a sky line on top of the data (which affected the subtraction), likely reduced the signal in this emission line. The low signal-to-noise ratio for A2 likely contributes to an error in redshift that causes the spectroscopic redshifts to differ beyond their estimated errors.

We use the REDMAPPER redshift  $z_{\text{lens}} = 0.4094 \pm 0.0189$  and the estimated source image–lens separation of  $\theta_{\text{sep}} = 4.46 \pm 0.71$  arcsec to calculate an enclosed mass of  $M_{\text{enc}} = (3.77 \pm 1.42) \times 10^{12} M_{\odot}$  for this system.

## 6 DISCUSSION AND SUMMARY

In this paper, we have presented new confirmations of galaxy-to-cluster-scale strong lenses in Y1 DES data. We first identified

candidates in DES data through an investigation of cluster sub-samples, and through catalogue searches of galaxies based on the photometry and proximity of lenses and source images. We then visually inspected these sub-samples to identify 46 candidates for a spectroscopic follow-up. The search was conducted over 1800 deg<sup>2</sup>. We confirmed these systems with spectroscopy from GMOS on the Gemini South telescope. The confirmed sample comprises three galaxy-scale lenses, five group-scale lenses, and one cluster-scale lens. They have been identified through known emission lines, such as Ly $\alpha$  and [O II] 3727. Of particular note is one system, DES J2321–4630, in which the presence of Ne emission lines suggests it may be a radio galaxy. For all the confirmed lenses, we provide a rough estimate of the lens mass based on an average of the source image–lens separation from Diehl17. Detailed modelling of these systems can contribute to studies of mass profiles and mass-to-light ratios of early-type galaxies. Poh et al. (in preparation) will report the modelling of a subset of these confirmed systems.

The redshift desert is a key problem in the spectroscopic follow-up of strong lenses. A number of our candidates could not be

confirmed or rejected, because they may exist in a redshift range not covered by GMOS spectrographs. One possible solution to this challenge is to seek improved photometric redshift estimations of high-redshift source galaxies. The measurement or prediction of photometric redshifts of distance objects is itself a long-time challenge, largely due to the small number of training sets at high redshift. Another solution is to perform observations in a higher wavelength range – e.g. in the (near-)infrared with Gemini South’s FLAMINGOS-2 instrument<sup>7</sup> and Paranal Observatory’s Very Large Telescope, which has MUSE and X-Shooter.<sup>8</sup>

The search in DES Y1 data and in that of Nord et al. (2016) produced many more candidates than feasibly can be followed up with modern spectroscopic observation resources. We confirmed fewer than of those we observed, with an observational strategy that efficiently used the available observing time. The best way to improve chances of positive spectroscopic confirmation in future work is to more accurately and precisely predict strong lens candidates from their imaging. Future searches of DES data are set to take place with more advanced algorithms, stemming from machine learning and citizen science programmes, among others. We expect that these algorithms will provide more flexibility, power, and efficiency in identifying high-quality strong lens candidates.

## ACKNOWLEDGEMENTS

We are grateful for the extraordinary contributions of our CTIO colleagues and the DES Camera, Commissioning, and Science Verification teams for achieving excellent instrument and telescope conditions that have made this work possible. The success of this project also relies critically on the expertise and dedication of the DES Data Management organization.

Funding for the DES Projects has been provided by the U.S. Department of Energy, the U.S. National Science Foundation, the Ministry of Science and Education of Spain, the Science and Technology Facilities Council of the United Kingdom, the Higher Education Funding Council for England, the National Center for Supercomputing Applications at the University of Illinois at Urbana-Champaign, the Kavli Institute of Cosmological Physics at the University of Chicago, the Center for Cosmology and Astro-Particle Physics at the Ohio State University, the Mitchell Institute for Fundamental Physics and Astronomy at Texas A&M University, Financiadora de Estudos e Projetos, Fundação Carlos Chagas Filho de Amparo à Pesquisa do Estado do Rio de Janeiro, Conselho Nacional de Desenvolvimento Científico e Tecnológico and the Ministério da Ciência e Tecnologia, the Deutsche Forschungsgemeinschaft, and the Collaborating Institutions in the DES. The DES data management system is supported by the National Science Foundation under Grant Number AST-1138766. The DES participants from Spanish institutions are partially supported by MINECO under grants AYA2012-39559, ESP2013-48274, FPA2013-47986, and Centro de Excelencia Severo Ochoa SEV-2012-0234, some of which include ERDF funds from the European Union.

The Collaborating Institutions are Argonne National Laboratory, the University of California at Santa Cruz, the University of Cambridge, Centro de Investigaciones Energéticas, Medioambientales y Tecnológicas-Madrid, the University of Chicago, University College London, the DES-Brazil Consortium, the Eidgenoessische

Technische Hochschule (ETH) Zurich, Fermi National Accelerator Laboratory, the University of Edinburgh, the University of Illinois at Urbana-Champaign, the Institut de Ciències de l’Espai (IEEC/CSIC), the Institut de Física d’Altes Energies, Lawrence Berkeley National Laboratory, the Ludwig-Maximilians Universität and the associated Excellence Cluster Universe, the University of Michigan, the National Optical Astronomy Observatory, the University of Nottingham, the Ohio State University, the University of Pennsylvania, the University of Portsmouth, the SLAC National Accelerator Laboratory, Stanford University, the University of Sussex, and Texas A&M University.

This work is based in part on observations obtained at the Gemini Observatory, which is operated by the Association of Universities for Research in Astronomy, Inc., under a cooperative agreement with the NSF on behalf of the Gemini partnership: the National Science Foundation (United States), the National Research Council (Canada), CONICYT (Chile), the Australian Research Council (Australia), Ministério da Ciência, Tecnologia e Inovação (Brazil), and Ministerio de Ciencia, Tecnología e Innovación Productiva (Argentina). The data were processed using the Gemini IRAF package v2.16.

This research has made use of NASA’s Astrophysics Data System.

This manuscript has been authored by Fermi Research Alliance, LLC under Contract No. DE-AC02-07CH11359 with the U.S. Department of Energy, Office of Science, Office of High Energy Physics. The United States Government retains and the publisher, by accepting the article for publication, acknowledges that the United States Government retains a non-exclusive, paid-up, irrevocable, worldwide license to publish or reproduce the published form of this manuscript, or allow others to do so, for United States Government purposes.

## REFERENCES

- Abazajian K. N. et al., 2009, *ApJS*, 182, 543
- Agnello A. et al., 2015, *MNRAS*, 454, 1260
- Agnello A. et al., 2017, *MNRAS*, 472, 4038A
- Bertin E., 2011, in Evans I. N., Accomazzi A., Mink D. J., Rots A. H., ASP Conf. Ser. Vol. 442, eds, Astronomical Data Analysis Software and Systems XX. Astron. Soc. Pac., San Francisco, p. 435
- Bertin E., Arnouts S., 1996, *A&AS*, 117, 393
- Blandford R. D., Narayan R., 1992, *ARA&A*, 30, 311
- Bonvin V. et al., 2017, *MNRAS*, 465, 4914
- Carlstrom J. E. et al., 2011, *PASP*, 123, 568
- Cawthon R. et al., 2017, *MNRAS*, 481, 2427C
- Collett T. E., 2015, *ApJ*, 811, 20
- Collett T. E., Auger M. W., Belokurov V., Marshall P. J., Hall A. C., 2012, *MNRAS*, 424, 2864
- Dark Energy Survey Collaboration et al., 2016, *MNRAS*, 460, 1270
- Diehl H. T. et al., 2009, *ApJ*, 707, 686
- Diehl H. T. et al., 2014, in Alison B. P., Chris R. B., Robert L. S., eds, Proc. SPIE Conf. Ser. Vol. 9149, The Dark Energy Survey and Operations: Year 1. SPIE, Bellingham, p. 91490V
- Diehl H. T. et al., 2017, *ApJS*, 232, 15
- Drlica-Wagner A. et al., 2018a, *ApJS*, 235, 33
- Drlica-Wagner A. et al., 2018b, *ApJS*, 235, 33
- Flaugher B. et al., 2015, *AJ*, 150, 150
- GAIA, 2015, Graphical Astronomy and Image Analysis Tool. Available at: <http://star-www.dur.ac.uk/pdraper/gaia/gaia.html> (accessed January 4 2017)
- Gavazzi R., Treu T., Koopmans L. V. E., Bolton A. S., Moustakas L. A., Burles S., Marshall P. J., 2008, *ApJ*, 677, 1046

<sup>7</sup><https://www.gemini.edu/sciops/instruments/flamingos2/>

<sup>8</sup><https://www.eso.org/public/usa/teles-instr/paranal-observatory/vlt/vlt-ins-tr/>, for example

- Hook I. M., Jørgensen I., Allington-Smith J. R., Davies R. L., Metcalfe N., Murowinski R. G., Crampton D., 2004, *PASP*, 116, 425  
 Humphrey A., Iwamuro F., Villar-Martín M., Binette L., Fosbury R., di Serego Alighieri S., 2007, *MNRAS*, 382, 1729  
 Ivezić Z. LSST Collaboration, et al., LSST Collaboration, 2008, *Serb. Astron. J.*, 176, 1  
 Jiang L. et al., 2014, *ApJS*, 213, 12  
 Kurtz M. J., Mink D. J., 1998, *PASP*, 110, 934  
 Lin H. et al., 2017, *ApJ*, 838, 15  
 Linder E. V., 2011, *Phys. Rev. D*, 84, 123529  
 Linder E. V., 2016, *Phys. Rev. D*, 94, 083510  
 More A. et al., 2012, *ApJ*, 749, 38  
 More A. et al., 2016, *MNRAS*, 455, 1191  
 Morganson E. et al., 2018, *PASP*, 130, 074501  
 Narayan R., Bartelmann M., 1996, preprint ([astro-ph/9606001](#))  
 Nord B. et al., 2016, *ApJ*, 827, 51  
 Oguri M., Marshall P. J., 2010, *MNRAS*, 405, 2579  
 Ostrovski F. et al., 2017, *MNRAS*, 465, 4325  
 Planck Collaboration XIII, 2015, *A&A*, 594, A13  
 Refsdal S., 1964, *MNRAS*, 128, 307  
 Rozo E. et al., 2016, *MNRAS*, 461, 1431  
 Rykoff E. S. et al., 2014, *ApJ*, 785, 104  
 Sánchez C. et al., 2014, *MNRAS*, 445, 1482  
 Sonnenfeld A., Gavazzi R., Suyu S. H., Treu T., Marshall P. J., 2013, *ApJ*, 777, 97  
 Suyu S. H. et al., 2017, *MNRAS*, 468, 2590  
 Tanaka M. et al., 2016, *ApJ*, 826, L19  
 Treu T., 2010, *ARA&A*, 48, 87  
 York D. G. SDSS Collaboration, et al., SDSS Collaboration, 2000, *AJ*, 120, 1579

- <sup>1</sup>Fermi National Accelerator Laboratory, PO Box 500, Batavia, IL 60510, USA  
<sup>2</sup>Kavli Institute for Cosmological Physics, University of Chicago, Chicago, IL 60637, USA  
<sup>3</sup>Department of Astronomy and Astrophysics, University of Chicago, Chicago, IL 60637, USA  
<sup>4</sup>Institute of Cosmology and Gravitation, University of Portsmouth, Portsmouth PO1 3FX, UK  
<sup>5</sup>European Southern Observatory, Karl-Schwarzschild-Strasse 2, D-85748 Garching, Germany  
<sup>6</sup>Department of Physics, ETH Zurich, Wolfgang-Pauli-Strasse 16, CH-8093 Zurich, Switzerland  
<sup>7</sup>Cerro Tololo Inter-American Observatory, National Optical Astronomy Observatory, Casilla 603, La Serena, Chile  
<sup>8</sup>Large Synoptic Survey Telescope, University of Arizona, 933 North Cherry Avenue, Tucson, AZ 85721, USA  
<sup>9</sup>Physics Department, 2320 Chamberlin Hall, University of Wisconsin-Madison, 1150 University Avenue Madison, WI 53706-1390, USA  
<sup>10</sup>Department of Physics and Astronomy, University College London, Gower Street, London WC1E 6BT, UK  
<sup>11</sup>Kavli Institute for Particle Astrophysics and Cosmology, PO Box 2450, Stanford University, Stanford, CA 94305, USA  
<sup>12</sup>SLAC National Accelerator Laboratory, Menlo Park, CA 94025, USA  
<sup>13</sup>Centro de Investigaciones Energéticas, Medioambientales y Tecnológicas (CIEMAT), E-28040 Madrid, Spain  
<sup>14</sup>Laboratório Interinstitucional de e-Astronomia – LIneA, Rua Gal. José Cristino 77, RJ-20921-400 Rio de Janeiro, Brazil  
<sup>15</sup>Department of Astronomy, University of Illinois at Urbana-Champaign, 1002 W. Green Street, Urbana, IL 61801, USA

- <sup>16</sup>National Center for Supercomputing Applications, 1205 West Clark St, Urbana, IL 61801, USA  
<sup>17</sup>Institut de Física d'Altes Energies (IFAE), The Barcelona Institute of Science and Technology, Campus UAB, E-08193 Bellaterra (Barcelona), Spain  
<sup>18</sup>Observatório Nacional, Rua Gal. José Cristiano 77, RJ-20921-400 Rio de Janeiro, Brazil  
<sup>19</sup>Department of Astronomy/Steward Observatory, 933 North Cherry Avenue, Tucson, AZ 85721-0065, USA  
<sup>20</sup>Jet Propulsion Laboratory, California Institute of Technology, 4800 Oak Grove Dr., Pasadena, CA 91109, USA  
<sup>21</sup>Department of Astronomy, University of Michigan, Ann Arbor, MI 48109, USA  
<sup>22</sup>Department of Physics, University of Michigan, Ann Arbor, MI 48109, USA  
<sup>23</sup>Institut d'Estudis Espacials de Catalunya (IEEC), E-08034 Barcelona, Spain  
<sup>24</sup>Institute of Space Sciences (ICE, CSIC), Campus UAB, Carrer de Can Magrans, s/n, E-08193 Barcelona, Spain  
<sup>25</sup>Instituto de Física Teórica UAM/CSIC, Universidad Autónoma de Madrid, E-28049 Madrid, Spain  
<sup>26</sup>Department of Physics, Stanford University, 382 Via Pueblo Mall, Stanford, CA 94305, USA  
<sup>27</sup>Santa Cruz Institute for Particle Physics, Santa Cruz, CA 95064, USA  
<sup>28</sup>Center for Cosmology and Astro-Particle Physics, The Ohio State University, Columbus, OH 43210, USA  
<sup>29</sup>Department of Physics, The Ohio State University, Columbus, OH 43210, USA  
<sup>30</sup>Max Planck Institute for Extraterrestrial Physics, Giessenbachstrasse, D-85748 Garching, Germany  
<sup>31</sup>Universitäts-Sternwarte, Fakultät für Physik, Ludwig-Maximilians Universität München, Scheinerstrasse 1, D-81679 München, Germany  
<sup>32</sup>Harvard-Smithsonian Center for Astrophysics, 60 Garden Street, Cambridge, MA 02138, USA  
<sup>33</sup>Australian Astronomical Optics, Macquarie University, North Ryde, NSW 2113, Australia  
<sup>34</sup>Departamento de Física Matemática, Instituto de Física, Universidade de São Paulo, CP 66318, SP-05314-970 São Paulo, Brazil  
<sup>35</sup>Department of Physics and Astronomy, University of Pennsylvania, Philadelphia, PA 19104, USA  
<sup>36</sup>George P. and Cynthia Woods Mitchell Institute for Fundamental Physics and Astronomy, Department of Physics and Astronomy, Texas A&M University, College Station, TX 77843, USA  
<sup>37</sup>Department of Astrophysical Sciences, Princeton University, Peyton Hall, Princeton, NJ 08544, USA  
<sup>38</sup>Institució Catalana de Recerca i Estudis Avançats, E-08010 Barcelona, Spain  
<sup>39</sup>Department of Physics and Astronomy, Pevenssey Building, University of Sussex, Brighton BN1 9QH, UK  
<sup>40</sup>School of Physics and Astronomy, University of Southampton, Southampton SO17 1BJ, UK  
<sup>41</sup>Physics Department, Brandeis University, 415 South Street, Waltham, MA 02453, USA  
<sup>42</sup>Instituto de Física Gleb Wataghin, Universidade Estadual de Campinas, 13083-859 Campinas, SP, Brazil  
<sup>43</sup>Computer Science and Mathematics Division, Oak Ridge National Laboratory, Oak Ridge, TN 37831, USA

This paper has been typeset from a TeX/LaTeX file prepared by the author.